DOI: 10.1478/AAPP.962A5

AAPP | Atti della Accademia Peloritana dei Pericolanti
Classe di Scienze Fisiche, Matematiche e Naturali
ISSN 1825-1242

Vol. 96, No. 2, A5 (2018)

MONODISPERSE MAGNETITE NANOPARTICLES WITH HIGH SENSITIVITY AS MRI CONTRAST AGENTS

ERNESTO AMATO [a], PAOLA LANZAFAME [b], ANTONIO ITALIANO [bc*], GIUSEPPE CICERO [a], GEORGIA PAPANIKOLAOU [b], SIGLINDA PERATHONER [d], GABRIELE CENTI [b] AND FABIO MINUTOLI [a]

ABSTRACT. The preparation of monodisperse and biocompatible water-soluble super-paramagnetic iron oxide nanoparticles (SPIONs) with high sensitivity in Magnetic Resonance Imaging (MRI) represents a challenge for the development of contrast agents. Here we report the synthesis of highly monodisperse citric acid (CA) coated SPIONs with an average diameter of 9 nm and spherical shape, prepared through a suitably optimized co-precipitation method. CA-SPIONs show a high solubility and stability in aqueous medium. Imaging of CA-SPIONs aqueous suspensions was performed in a clinical 1.5-T MRI scanner and different clinical acquisition sequences were exploited. Results show that image contrast can be effectively improved when concentrations of SPIONs lower than 1 ppm are present, and that the echo time is the main parameter influencing the image contrast of SPION-loaded solutions. Moreover, we found that CA-SPIONs show a high value of transverse relaxivity of 128 L mmol^{-1} s^{-1} (higher than the commercial contrast agents). Our results are encouraging for the further development of clinical application of SPIONs in MRI, and can represent a starting point for the optimization of clinical imaging exploiting the contrast enhancement of such agents. Namely, it seems possible to achieve an optimal image contrast with low concentration of SPIONs; this could lead to a lower probability of side effects.

1. Introduction

Precision medicine incresingly exploits molecular approaches for the diagnosis and therapy of several diseases. Specific molecular targets can be localized only using high sensitivity *in vivo* imaging techniques. To this aim, nuclear medicine provides the most sensitive technique to locate molecular targets. However, it suffers from low spatial resolution and is charged by the use of ionizing radiation. Magnetic Resonance Imaging (MRI) does not use ionizing radiation and is a multi-parametric, large field-of-view technique which can show high sensitivity for molecular targets (Bakhtiary *et al.* 2016). Among MRI contrast agents, it has been demonstrated that better sensitivity can be obtained by using super-paramagnetic iron oxide nanoparticle (SPIONs) contrast media (Shokrollahi 2013a; Adamson *et al.* 2017). More generally, SPIONs have attracted a growing attention

in recent years thanks to their potential biomedical applications including - besides MRI - also magnetic hyperthermia and drug delivery (Corot *et al.* 2006; Laurent and Mahmoudi 2011; Kai *et al.* 2017; Yu *et al.* 2017).

The large-scale synthesis of SPIONs with high crystallinity and high magnetization at saturation requires a reproducible and industrial process without any laborious purification step, in order to ensure cost-effective synthetic procedures (Barrow *et al.* 2016). Such contrast agents can be engineered properly in order to bound specific targets (Rapley *et al.* 2012; Nam *et al.* 2013; Maggioni *et al.* 2014; Sundaresan *et al.* 2014; Mao *et al.* 2016; Galli *et al.* 2017), even if a certain number of issues still remains to be addressed before a full clinical adoption (Antonelli *et al.* 2013; Schleich *et al.* 2015).

Toxicity induced in organ tissues inevitably depend on a series of interrelated parameters. Consequently, recent studies, aimed to evaluate the possible effects of biocompatibility and toxicity attributable to SPIONs, have been carried out for different cell types in human organs keeping into account different concentrations and for a wide set of coating materials and exposure times (Hong *et al.* 2011; Patil *et al.* 2018). Exposure time, as well as concentration, have been shown to play a crucial role in toxicity of SPIONs: a high dose exposure can produce a severe cellular stress, while concentration, also depending on the involved organ, does not cause undesired effects if kept under a proper threshold. It has been also observed (Faux *et al.* 1992) that *in vivo* studies on administration of dietary iron in rats increased the number of DNA breaks revealing a possible source of genotoxicity; on the other hand, data on immunotoxicity effects due to SPIONs are to date not enough to ensure an interaction between SPIONs and immune system. Anyway, the toxicity effects due to SPIONs are currently under control in several facets, bearing in mind the optimization of all the parameters to minimize DNA damage, oxidative stress and mitochondrial membrane dysfunction, to guarantee as large as possible biocompatibility.

Among the several features influencing the capability of magnetic resonance (MR) scanners to detect SPIONs (Shokrollahi 2013b; Basini *et al.* 2017), particle size, oxidation state, concentration and the transverse relaxivity (Muller *et al.* 1991) are the main ones to which the contrast-enhancing effect of SPIONs in MRI can be ascribed; another feature affecting image quality is represented by the choice of the proper MR sequence (Nam *et al.* 2013; Adamson *et al.* 2017; Knopp *et al.* 2017).

Aim of the present work was to synthesize and characterize SPIONs with high transverse relaxivity and to optimize their detectability and related image contrast, using a clinical MRI scanner, with different clinical MR sequences.

2. Materials and methods

2.1. Nanoparticle preparation and characterization. Citric acid (CA) coated nanoparticles were synthesized using a slight modification of the coprecipitation method reported by Narayanan *et al.* (2011); 0.01 mol of $FeCl_3 \cdot 6H_2O$ and 0.05 mol of $FeSO_4 \cdot 7H_2O$ were dissolved in 10 ml of deionized water under argon in a three-necked flask. Sixteen milliliters of NH_4OH solution ($\geq 25\%$) were added drop-wise to the metal solution with vigorous and continuous stirring over a period of 20 minutes. The colour shift of the solution from orange to black is a signature of the formation of magnetite particles. A solution containing 0.5 g of citric acid in 1.5 ml of distilled water was then added dropwise to the previously prepared

solution and then the solution was kept at 65°C for 1 hour. The solvent was removed by magnetic decantation and the particles (CA-SPIONs) were washed twice in water; a proper amount of the precipitate was dispersed in water by intensive ultrasonication, to obtain a well dispersed and stable solution.

Another part of the precipitate was dried in a vacuum oven at 50°C for solid phase characterization. The dried precipitate was characterized by X-ray diffraction (XRD) for structural determination and estimation of crystallite size in a Bruker D2 Phaser desktop diffractometer equipped with a Cu tube ($\lambda = 1.54056$ Å), recording the data in the 2ϑ range of $20^\circ - 80^\circ$ with an angular step size of 0.025°. The average crystallite size of Fe_3O_4 is calculated by X-ray diffraction line broadening using the Debye Scherrer formula:

$$d = \frac{\kappa\lambda}{\beta\cos\theta} \tag{1}$$

where d represents the grain size; $\kappa = 1$ is the Scherrer constant related to the shape and index (hkl) of the crystals; λ is the wavelength of the X-ray (CuK_α, 1.54056 Å); ϑ is the diffraction angle of the peak; β stands for the full width at half-height of the peaks (in radians). The morphology of samples was analyzed using a JEOL JEM 2010 TEM microscope operating at 200 kV. The infra-red spectra were recorded in the range 4000-400 cm^{-1} using a Thermo FTIR Nicolet iS50 spectrometer with a MCT detector.

2.2. MRI measurements. The prepared SPIONs were diluted in distilled water samples, at different concentrations. Cylindrical test tubes containing the samples were placed in a parallelepiped phantom filled with pure water, and imaged with a 1.5 T superconducting MRI scanner (PHILIPS 1.5T MR Achieva) using a brain coil. The per cent contrast index, $CI(\%)$, on sample images was evaluated as:

$$CI = 100 \cdot \frac{I_s - I_w}{I_w} \tag{2}$$

where I_s and I_w are the image intensities for each sample and for water, respectively. I_s was evaluated drawing a circular region of interest (ROI) on the median plane of the sample, with a diameter of about 2/3 the tube diameter, while I_w was estimated as average of four measurements taken at the four cardinal points surrounding the doped sample. Various sequences were adopted in order to focus the optimal performance: gradient-echo (GE), spin-echo (SE) and turbo spin-echo (TSE), for different combinations of parameters: repetition time (TR), echo-time (TE) and flip angle (FA). Table 1 summarizes all the experimental measurements carried out for the various sets of parameters.

The first sequence studied was the gradient-echo one. For this sequence, and for each SPION concentration χ, different (TE, FA) combinations were adopted: $TE = 23, 37$ and 46 ms for $FA = 18^\circ$, $TE = 46$ ms for $FA = 8^\circ$ and 38°. The second sequence employed was the turbo spin-echo one, choosing for TE the values of $120, 250$ and 500 ms, and a flip angle of 90°. Finally, the SE sequence was tested, with a $FA = 90^\circ$ and a double value of $TE = 50, 200$ ms. These last results were used to calculate, following the approach described by Rohrer *et al.* (2005), the transverse relaxation times T_2, as:

$$SI(TE) = SI_0 \cdot e^{-TE/T_2} + SI_{noise} \tag{3}$$

TABLE 1. MRI sequences adopted on the 1.5 T scanner, for different combinations of *TR*, *TE* and *FA* acquisition parameters.

sequence	*TR* (ms)	*TE* (ms)	*FA*	slices	acq. matrix	acq. time (s)
GE	722	23	18°	23	232×146	451
GE	722	37	18°	23	232×146	451
GE	722	46	18°	23	232×146	300
GE	722	46	8°	23	232×146	150
GE	722	46	38°	23	232×146	150
TSE	3000	120	90°	11	168×132	438
TSE	3000	250	90°	11	168×132	876
TSE	3000	500	90°	11	168×132	1314
SE	2000	50/200[(a)]	90°	3	256×205	190

[(a)] double

where $SI(TE)$ is the signal intensity as a function of the echo time *TE*, SI_0 is the steady-state *SI* and SI_{noise} is the noise level of signal. For each experimental sample, *i.e.*, for each SPION concentration in water, the T_2 relaxivity, r_2, was evaluated as:

$$r_2 = \frac{1}{\chi}\left(\frac{1}{T_2} - \frac{1}{T_2^w}\right) \tag{4}$$

The relaxivity is expressed in $\mathrm{L\,mmol^{-1}\,s^{-1}}$, when the concentration of Fe ions (magnetic centers) is in $\mathrm{mmol\,L^{-1}}$, and the sample and water transverse relaxation times, T_2 and T_2^w respectively, are in seconds.

3. Results and discussion

3.1. Characterization of citric acid-coated Fe_3O_4 nanoparticles. The XRD pattern of the powered sample (see Fig. 1) evidenced the reflections at $2\vartheta = 30.3°$, 35.7°, 43.4°, 53.8°, 57.5°, 63.1°, 74.8°, that are indexed as (220), (311), (400), (422), (511), (440) and (533) crystal planes of the Fe_3O_4. All these diffraction peaks are typical of the face-centred cubic (FCC) crystalline structure of Fe_3O_4, in accordance with that of the standard spectrum (COD 1011032). The peaks appear broader because of the reduced particle size; the average diameter of CA-SPIONs, calculated by the Debye Scherrer equation from the (311) peak, is about 10 nm. The presence of Fe_3O_4 phase was further confirmed by XPS results. In the Fe 2p region, the main peaks are at 711.1 eV ($2p_{3/2}$), for both oxidation states Fe^{3+} and Fe^{2+}, and at 724.6 eV ($2p_{1/2}$), for Fe^{3+} (Márquez *et al.* 2011). A $Fe^{2+}:Fe^{3+}$ ratio near to 1 : 2 was obtained by deconvolution of the corresponding peaks, confirming the formation of Fe_3O_4.

Size and morphology of CA-SPIONs were examined by transmission electron microscopy (TEM). In Fig. 2(a) the electron micrograph image of CA-SPIONs evidences a roughly spherical morphology without aggregation of the nanoparticles, while Fig. 2(b) shows a narrow-size distribution ranging from 3 to 14 nm, with a dominant population

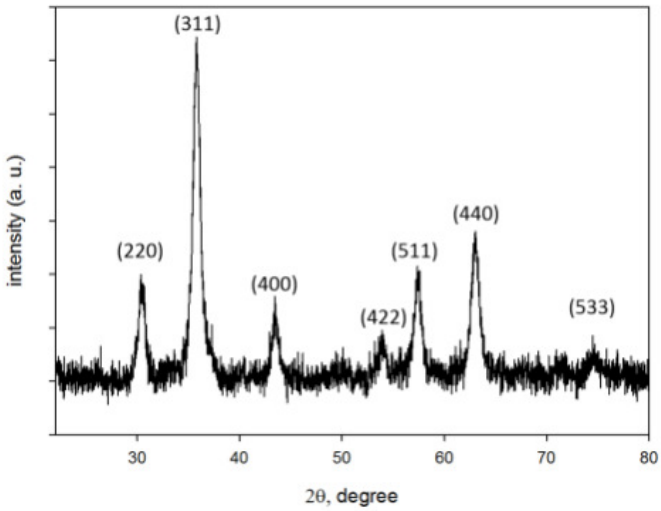

FIGURE 1. XRD pattern of CA-SPIONs.

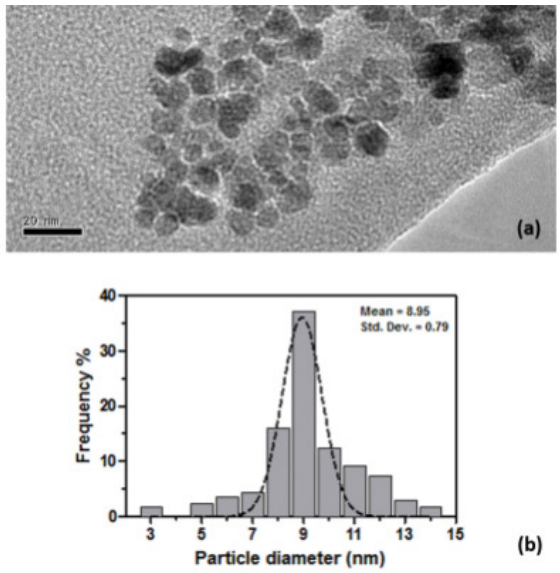

FIGURE 2. (a) TEM image of SPIONs; (b) histogram of size distribution of CA-SPIONs.

around 9 nm (38%), in agreement with the Debye Scherrer equation. Figure 3 shows the FTIR spectra of pure CA and CA-SPIONs: CA spectrum presents well resolved absorption bands, whereas CA-SPION spectrum exhibits a smaller number of bands, characterized

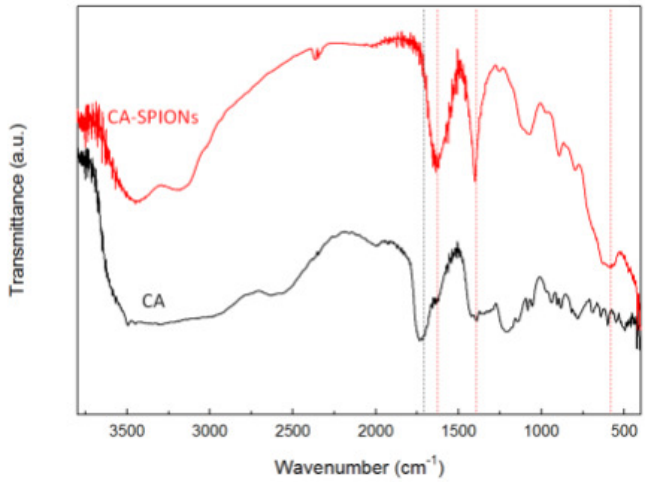

FIGURE 3. FTIR spectra of pure CA and CA-SPIONs.

by a larger width. The 1720 cm^{-1} peak can be associated to the asymmetric stretching of C=O bond from the carboxylic group of CA. This peak shifts to 1620 cm^{-1} in CA-SPIONs sample due to the partial single bond character of C=O as a results of the CA binding to the surface of Fe_3O_4 nanoparticles (Sahoo *et al.* 2005). Furthermore, the vibrational mode at 1396 cm^{-1} can be ascribed to the symmetric stretching of COO-group of citric acid (Max and Chapados 2004). The strong absorption peak at around 583 cm^{-1} can be attributed to the Fe-O stretching vibrations in Fe_3O_4 nanoparticles. Usually the Fe-O stretching vibration band of the bulk magnetite is around 570 cm^{-1} but, in our case, the observed band shifts to higher wave-numbers due to the finite size of nanoparticles (Ma *et al.* 2003).

3.2. Evaluation of contrast index in MRI. Figure 4 shows an example of MR image acquired using a turbo spin-echo sequence on our phantom; all images were then analysed as described in the previous section, in order to determine the contrast index. Our measurements are reported as plots in Figs. 5, 6 and 7, illustrating *CI* versus SPION concentration χ of our samples. For all sequences it is evident the effectiveness of SPIONs in enhancing image contrast, clearly allowing to distinguish the contrast-loaded sample with respect to the background.

Concerning GE sequences, as described by Fig. 5, the value of *CI* around -80% is obtained for different concentrations: $\chi = 5$ ppm for $TE = 46$ ms and $FA = 8°, 18°$ or $38°$, $\chi = 8$ ppm for $TE = 37$ ms and $FA = 18°$, $\chi = 10$ ppm for $TE = 23$ ms and $FA = 18°$. Spin-echo sequence, using a 50 ms *TE*, gives the worst *CI* at all concentrations, as shown in Fig. 6. On the other hand, using a 200 ms *TE*, a high *CI* of -80% is reached at 5 ppm, as the best performing GE sequence. Finally, a TSE sequence (see Fig. 7) appears the most

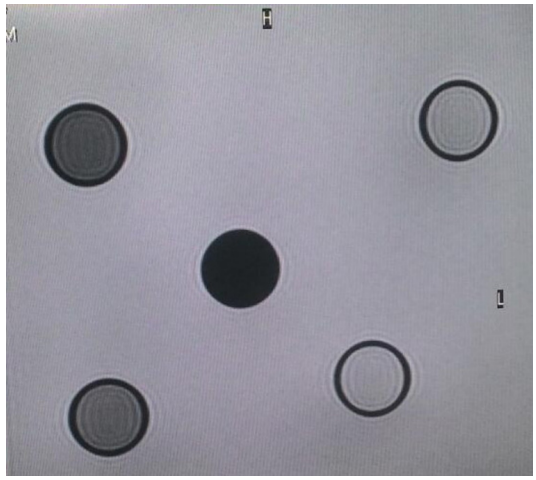

FIGURE 4. Images obtained by a TSE sequence of solutions containing SPIONs, for $\chi = 0.2, 0.5, 1, 2$ and 5 ppm, increasing from the lightest to the darkest, in a pure water phantom.

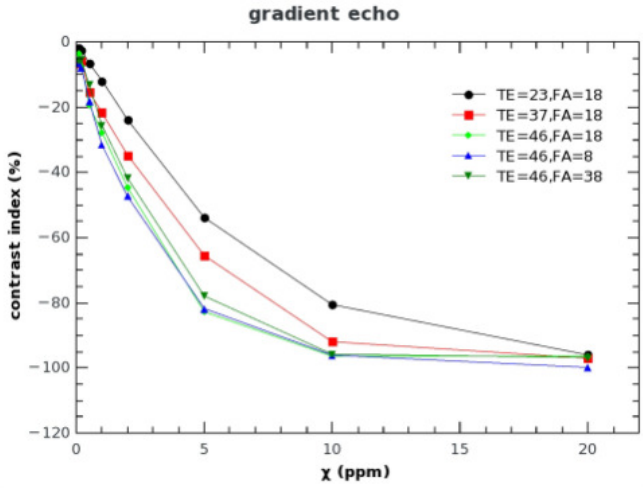

FIGURE 5. Contrast index (*CI*) *vs.* SPION concentration χ when a GE sequence is adopted for different (TE, FA) combinations.

promising one. As a matter of fact, *CI* drops rapidly down to -80% for $TE = 500$ ms and a concentration $\chi = 1$ ppm, or, similarly, for $TE = 250$ ms and a concentration of $\chi = 2$ ppm; conversely, the third adopted echo time, $TE = 120$ ms, would require a concentration

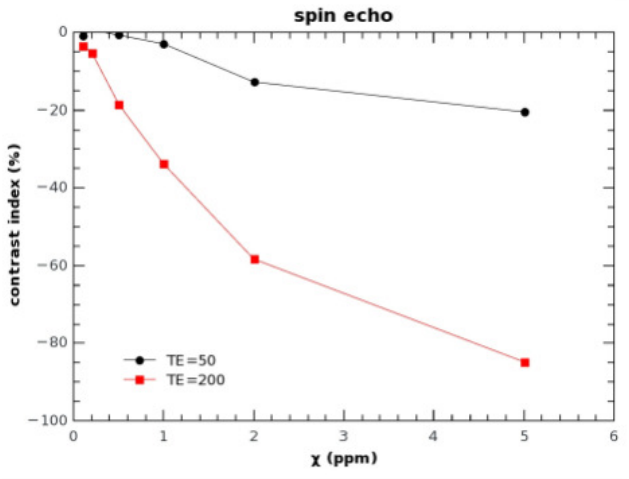

FIGURE 6. Contrast index (*CI*) *vs*. SPION concentration χ when an SE sequence is adopted for different *TE* values and for a *FA* = 90°.

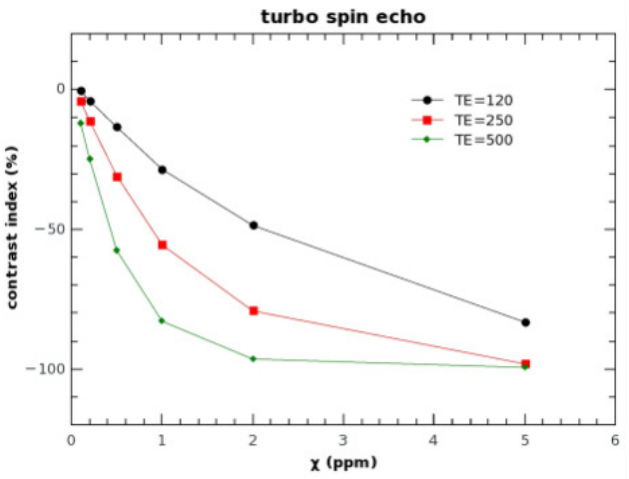

FIGURE 7. Contrast index (*CI*) *vs*. SPION concentration when a TSE sequence is adopted for different *TE* values and for a *FA* = 90°.

χ = 5 ppm. Transverse relaxation times T_2 and relaxivity r_2 were calculated, relying on SE imaging, following the approach described in the previous section.

TABLE 2. T_2 relaxation rates and relaxivity for the various tested concentrations.

χ (ppm)	0.1	0.2	0.5	1	2	5
χ (mmol L^{-1})	1.79E-03	3.58E-03	8.95E-03	1.79E-02	3.58E-02	8.95E-02
$1/T_2$ (s^{-1})	1.384	1.566	2.478	3.765	6.101	12.225
$1/T_2 - 1/T_2^w$ (s^{-1})	0.197	0.380	1.291	2.579	4.915	11.038
r_2 (L mmol^{-1} s^{-1})	110	106	144	144	137	123

Table 2 reports these results, while Fig. 8 shows the linear relationship between the difference of relaxation rates and the solution concentration. When comparing these results with those reported by Rohrer *et al.* (2005) about T_2-weighted imaging in a clinical 1.5-Tesla scanner of water solutions of the commercial super-paramagnetic contrast media Resovist© and Feridex/Endorem©, one sees that the average r_2 obtained for our samples ((128 ± 17) L mmol^{-1} s^{-1}) is higher than the corresponding values reported for Resovist (61 L mmol^{-1} s^{-1}) and Feridex/Endorem (41 L mmol^{-1} s^{-1}). The high value of r_2 relaxivity of our SPION samples enabled us to obtain significant contrast in very diluted solutions, characterized by concentrations ranging from 8.9×10^{-2} mmol L^{-1} (5 ppm) to as low as 1.8×10^{-3} mmol L^{-1} (0.1 ppm). In comparison, Rohrer *et al.* (2005) employed dilutions of SPION contrast media ranging from 0.5 to 0.1 mmol L^{-1}. Our results are also quite encouraging in comparison with those ones exhibited by far larger SPIO nano-clusters of 64 nm diameter (Xu *et al.* 2012) that, in a clinical 1.5-T MRI scanner, have shown a r_2 value of about 650 L mmol^{-1} s^{-1}, but using particles seven times larger in diameter.

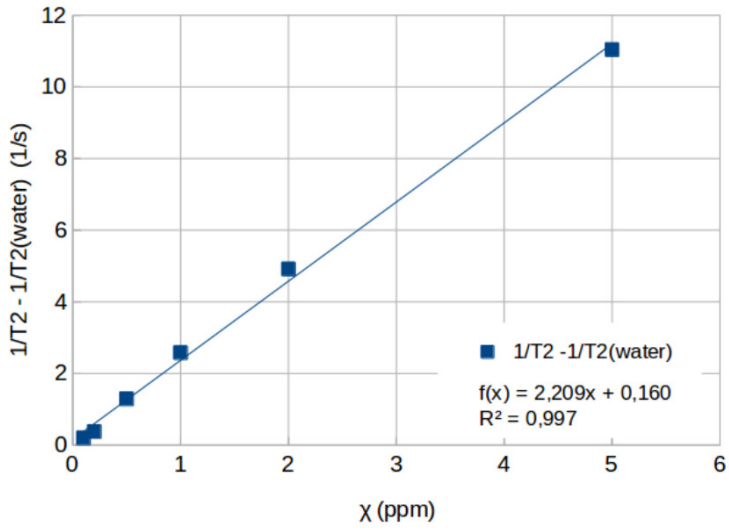

FIGURE 8. Plot of the difference between SPION solution and water relaxation rates as a function of the concentrations, resulting from imaging with an SE sequence.

4. Conclusions

Through an optimized co-precipitation method, highly mono-disperse SPIONs were synthesized. XRD characterization identifies Magnetite as the unique crystalline phase in our SPIONs. TEM results point out the uniformity in shape and size ($\sim$ 9 nm) of the obtained particles; furthermore, due to the stabilization of the surface by adsorption of citric acid, SPIONs show a high solubility and stability in water solution, suitable properties for biomedical applications. Our study shows that the prepared SPIONs are able to enhance the signal intensity also when highly diluted, using commercial MR scanners and sequences. We highlight that *TE* is the most crucial parameter influencing the contrast index (*i.e.*, the detectability of lesions potentially targeted by SPIONs) whereas the sequence kind and flip angle are far less important. These results are encouraging for further development of clinical application of SPIONs in MRI, and can represent a starting point for the optimization of clinical imaging exploiting the contrast enhancement of such agents. Namely, it seems possible to achieve an optimal image contrast with low concentration of SPIONs; this leads to a lower probability of incidence of relevant side effects, such as anaphylaptic shocks, sometimes lethal.

References

Adamson, E. B., Ludwig, K. D., Mummy, D. G., and Fain, S. B. (2017). "Magnetic resonance imaging with hyperpolarized agents: Methods and applications". *Physics in Medicine and Biology* **62**(13), R81–R123. DOI: 10.1088/1361-6560/aa6be8.

Antonelli, A., Sfara, C., Battistelli, S., Canonico, B., Arcangeletti, M., Manuali, E., Salamida, S., Papa, S., and Magnani, M. (2013). "New strategies to prolong the in vivo life span of iron-based contrast agents for MRI". *PLoS ONE* **8**(10). DOI: 10.1371/journal.pone.0078542.

Bakhtiary, Z., Saei, A. A., Hajipour, M. J., Raoufi, M., Vermesh, O., and Mahmoudi, M. (2016). "Targeted superparamagnetic iron oxide nanoparticles for early detection of cancer: Possibilities and challenges". *Nanomedicine: Nanotechnology, Biology, and Medicine* **12**(2), 287–307. DOI: 10.1016/j.nano.2015.10.019.

Barrow, M., Taylor, A., García Carrión, J., Mandal, P., Park, B. K., Poptani, H., Murray, P., Rosseinsky, M. J., and Adams, D. J. (2016). "Co-precipitation of DEAE-dextran coated SPIONs: how synthesis conditions affect particle properties, stem cell labelling and MR contrast". *Contrast Media and Molecular Imaging* **11**(5), 362–370. DOI: 10.1002/cmmi.1700.

Basini, M., Orlando, T., Arosio, P., Casula, M. F., Espa, D., Murgia, S., Sangregorio, C., Innocenti, C., and Lascialfari, A. (2017). "Local spin dynamics of iron oxide magnetic nanoparticles dispersed in different solvents with variable size and shape: A ^{1}H NMR study". *Journal of Chemical Physics* **146**(3). DOI: 10.1063/1.4973979.

Corot, C., Robert, P., Idée, J.-M., and Port, M. (2006). "Recent advances in iron oxide nanocrystal technology for medical imaging". *Advanced Drug Delivery Reviews* **58**(14), 1471–1504. DOI: 10.1016/j.addr.2006.09.013.

Faux, S. P., Francis, J. E., Smith, A. G., and Chipman, J. K. (1992). "Induction of 8-hydroxydeoxyguanosine in *Ah*-responsive mouse liver by iron and Aroclor 1254". *Carcinogenesis* **13**(2), 247–250. DOI: 10.1093/carcin/13.2.247.

Galli, M., Guerrini, A., Cauteruccio, S., Thakare, P., Dova, D., Orsini, F., Arosio, P., Carrara, C., Sangregorio, C., Lascialfari, A., Maggioni, D., and Licandro, E. (2017). "Superparamagnetic iron oxide nanoparticles functionalized by peptide nucleic acids". *RSC Advances* **7**(25), 15500–15512. DOI: 10.1039/c7ra00519a.

Hong, S. C., Lee, J. H., Lee, J., Kim, H. Y., Park, J. Y., Cho, J., Lee, J., and Han, D. W. (2011). "Subtle cytotoxicity and genotoxicity differences in superparamagnetic iron oxide nanoparticles coated with various functional groups." *International Journal of Nanomedicine* **6**, 3219–3231. DOI: 10.2147/IJN.S26355.

Kai, L., Nejadnik, H., and Daldrup-Link, H. E. (2017). "Next-generation superparamagnetic iron oxide nanoparticles for cancer theranostics". *Drug Discovery Today* **22**(9), 1421–1429. DOI: 10.1016/j.drudis.2017.04.008.

Knopp, T., Gdaniec, N., and Möddel, M. (2017). "Magnetic particle imaging: From proof of principle to preclinical applications". *Physics in Medicine and Biology* **62**(14), R124–R178. DOI: 10.1088/1361-6560/aa6c99.

Laurent, S. and Mahmoudi, M. (2011). "Superparamagnetic iron oxide nanoparticles: Promises for diagnosis and treatment of cancer". *International Journal of Molecular Epidemiology and Genetics* **2**(4), 367–390. URL: http://ijmeg.org/IJMEG1111002A.html.

Ma, M., Zhang, Y., Yu, W., Shen, H. Y., Zhang, H. Q., and Gu, N. (2003). "Preparation and characterization of magnetite nanoparticles coated by amino silane". *Colloids and Surfaces A: Physicochemical and Engineering Aspects* **57**, 1149–1179. DOI: 10.1016/S0927-7757(02)00305-9.

Maggioni, D., Arosio, P., Orsini, F., Ferretti, A. M., Orlando, T., Manfredi, A., Ranucci, E., Ferruti, P., D'Alfonso, G., and Lascialfari, A. (2014). "Superparamagnetic iron oxide nanoparticles stabilized by a poly(amidoamine)-rhenium complex as potential theranostic probe". *Dalton Transactions* **43**(3), 1172–1183. DOI: 10.1039/c3dt52377b.

Mao, X., Xu, J., and Cui, H. (2016). "Functional nanoparticles for magnetic resonance imaging". *Wiley Interdisciplinary Reviews: Nanomedicine and Nanobiotechnology* **8**(6), 814–841. DOI: 10.1002/wnan.1400.

Márquez, F., Campo, T., Cotto, M., Polanco, R., Roque, R., Fierro, P., Sanz, J., Elizalde, E., and Morant, C. (2011). "Synthesis and characterization of monodisperse magnetite hollow microspheres". *Soft Nanoscience Letters* **1**(2), 25–32. DOI: 10.4236/snl.2011.12005.

Max, J. J. and Chapados, C. (2004). "Infrared spectroscopy of aqueous carboxylic acids: comparison between different acids and their salts". *Journal of Physical Chemistry A* **108**, 3324–3337. DOI: 10.1021/jp036401t.

Muller, R. N., Gillis, P., Moiny, F., and Roch, A. (1991). "Transverse relaxivity of particulate MRI contrast media: From theories to experiments". *Magnetic Resonance in Medicine* **22**(2), 178–182. DOI: 10.1002/mrm.1910220203.

Nam, J., Won, N., Bang, J., Jin, H., Park, J., Jung, S., Jung, S., Park, Y., and Kim, S. (2013). "Surface engineering of inorganic nanoparticles for imaging and therapy". *Advanced Drug Delivery Reviews* **65**(5), 622–648. DOI: 10.1016/j.addr.2012.08.015.

Narayanan, T. N., Reena Mary, A. P., Swalih, P. K. A., Kumar, D. S., Makarov, D., Albrecht, M., Puthumana, J., Anas, A., and Anantharam, M. R. (2011). "Enhanced bio-compatibility of ferrofluids of self-assembled superparamagnetic iron oxide-silica core-shell nanoparticles". *Journal of Nanoscience and Nanotechnology* **65**, 1958–1967. DOI: 10.1166/jnn.2011.3578.

Patil, R. M., Thorat, N. D., Shete, P. B., Bedge, P. A., Gavde, S., Joshi, M. G., Tofail, S. A., and Bohara, R. A. (2018). "Comprehensive cytotoxicity studies of superparamagnetic iron oxide nanoparticles". *Biochemistry and Biophysics Reports* **13**, 63–72. DOI: 10.1016/j.bbrep.2017.12.002.

Rapley, P. L., Witiw, C., Rich, K., Niccoli, S., Tassotto, M. L., and Thng, J. (2012). "*In vitro* molecular magnetic resonance imaging detection and measurement of apoptosis using superparamagnetic iron oxide + antibody as ligands for nucleosomes". *Physics in Medicine and Biology* **57**(21), 7015. DOI: 10.1088/0031-9155/57/21/7015.

Rohrer, M., Bauer, H., Mintorovitch, J., Requardt, M., and Weinmann, H. J. (2005). "Comparison of magnetic properties of MRI contrast media solutions at different magnetic field strengths". *Investigative Radiology* **40**, 715–724. DOI: 10.1097/01.rli.0000184756.66360.d3.

Sahoo, Y., Goodarzi, A., Swihart, M. T., Ohulchanskyy, T. Y., Kaur, N., Furlani, E. P., and Prasad, P. N. (2005). "Aqueous ferrofluid of magnetite nanoparticles: fluorescence labeling and magnetophoretic control". *Journal of Physical Chemistry B* **109**, 3879–3885. DOI: 10.1021/jp045402y.

Schleich, N., Danhier, F., and Préat, V. (2015). "Iron oxide-loaded nanotheranostics: Major obstacles to in vivo studies and clinical translation". *Journal of Controlled Release* **198**, 35–54. DOI: 10.1016/j.jconrel.2014.11.024.

Shokrollahi, H. (2013a). "Contrast agents for MRI". *Materials Science and Engineering C* **33**(2), 4485–4497. DOI: 10.1016/j.msec.2013.07.012.

Shokrollahi, H. (2013b). "Structure, synthetic methods, magnetic properties and biomedical applications of ferrofluids". *Materials Science and Engineering C* **33**(5), 2476–2487. DOI: 10.1016/j.msec.2013.03.028.

Sundaresan, V., Menon, J. U., Rahimi, M., Nguyen, K. T., and Wadajkar, A. S. (2014). "Dual-responsive polymer-coated iron oxide nanoparticles for drug delivery and imaging applications". *International Journal of Pharmaceutics* **466**(1-2), 1–7. DOI: 10.1016/j.ijpharm.2014.03.016.

Xu, F., Cheng, C., Chen, D.-X., and Gu, H. C. (2012). "Magnetite nanocrystal clusters with ultra-high sensitivity in magnetic resonance imaging". *ChemPhysChem* **13**, 336–341. DOI: 10.1002/cphc.201100548.

Yu, E. Y., Bishop, M., Zheng, B., Ferguson, R. M., Khandhar, A. P., Kemp, S. J., Krishnan, K. M., Goodwill, P. W., and Conolly, S. M. (2017). "Magnetic particle imaging: A novel in vivo imaging platform for cancer detection". *Nano Letters* **17**(3), 1648–1654. DOI: 10.1021/acs.nanolett.6b04865.

---

[a] Università degli Studi di Messina
Dipartimento di Scienze Biomediche, Odontoiatriche e delle Immagini Morfologiche e Funzionali
Via Consolare Valeria, 98125 Messina (Italy)

[b] Università degli Studi di Messina
Dipartimento di Scienze Matematiche e Informatiche, Scienze Fisiche e Scienze della Terra
Via Stagno d'Alcontres, 98166 Messina (Italy)

[c] Istituto Nazionale di Fisica Nucleare
Sezione di Catania, Catania (Italy)

[d] Università degli Studi di Messina
Dipartimento di Scienze Chimiche, Biologiche, Farmaceutiche e Ambientali
Via Stagno d'Alcontres, 98166 Messina (Italy)

[*] To whom correspondence should be addressed | email: antonio.italiano@ct.infn.it

Communicated 20 June 2018; manuscript received 26 June 2018; published online 28 November 2018